Density imaging using inverse scattering

Roberto J. Lavarello[a] and Michael L. Oelze
Bioacoustics Research Laboratory, Department of Electrical and Computer Engineering, University of Illinois at Urbana-Champaign, 405 North Matthews, Urbana, Illinois 61801

(Received 20 February 2008; revised 6 October 2008; accepted 11 November 2008)

Inverse scattering is considered one of the most robust and accurate ultrasonic tomography methods. Most inverse scattering formulations neglect density changes in order to reconstruct sound speed and acoustic attenuation. Some studies available in literature suggest that density distributions can also be recovered using inverse scattering formulations. Two classes of algorithms have been identified. (1) The separation of sound speed and density contributions from reconstructions using constant density inverse scattering algorithms at multiple frequencies. (2) The inversion of the full wave equation including density changes. In this work, the performance of a representative algorithm for each class has been studied for the reconstruction of circular cylinders: the dual frequency distorted Born iterative method (DF-DBIM) and the *T*-matrix formulation. Root mean square error values lower than 30% were obtained with both algorithms when reconstructing cylinders up to eight wavelengths in diameter with moderate density changes. However, in order to provide accurate reconstructions the DF-DBIM and *T*-matrix method required very high signal-to-noise ratios and significantly large bandwidths, respectively. These limitations are discussed in the context of practical experimental implementations.
 [DOI: 10.1121/1.3050249]

PACS number(s): 43.35.Wa, 43.60.Pt [TDM] Pages: 793–802

I. INTRODUCTION

Ultrasonic computerized tomography (UCT) is an imaging modality used to reconstruct quantitative images of acoustic properties and has been studied since the 1970s. Initial attempts were performed using ray propagation algorithms to form images of attenuation α (Ref. 1) and speed of sound c (Ref. 2). These algorithms can only correct for refraction and their spatial resolution is limited by diffraction effects. Diffraction tomography was developed in the 1980s as a means to compensate for diffraction effects by linearizing the wave equation using either the Born or Rytov approximations, but this approach provides erroneous solutions even for low contrast between the acoustic properties of the background and the scattering object.[3]

Traditionally, inverse scattering algorithms in the frequency domain based on Newton-type approaches such as the distorted Born iterative method (DBIM)[4,5] attempt to solve for the full wave equation assuming no changes in density ρ. Under this assumption, these algorithms allow the reconstruction of c and α. Newton-type inverse scattering algorithms are not limited by diffraction effects, and convergence for large contrast objects can be obtained by properly using multiple frequency data.[6]

However, experimental evidence is available in literature suggesting that relative ρ changes in tissues may be comparable in magnitude to relative c changes.[7,8] The effects of variable density in the reconstruction of sound speed were observed to result in overshoots of sound speed estimates at the edges of objects where density underwent abrupt changes.[9] Sharper changes in density were found to lead to larger artifacts in reconstructed images of sound speed.

Currently, UCT has been proposed for the early detection and diagnosis of breast cancer. Clinical trials indicate that α reconstructions may be more important than c reconstructions for differentiating benign from malignant lesions.[10] Determining density distributions may provide additional information or contrast for cancer detection.

Quantitative ultrasound techniques based on the backscatter (QUBS) may also benefit from the determination of density distributions.[11] QUBS consists of estimating properties of tissue microstructure based on backscattered pressure measurements and scattering models. Under weak scattering assumptions, the backscattered power spectrum can be related to the three-dimensional spatial autocorrelation function of the acoustic impedance, $Z=\rho c$, of the underlying tissue microstructure.[12] Therefore, using variable density UCT in conjunction with c reconstructions at high frequencies could in theory be useful for QUBS by providing three-dimensional impedance maps of tissues.

The number of UCT studies that consider variable density is limited. Variable density UCT was introduced in the context of single scattering formulations using bistatic scanning configurations with infinite bandwidth transducers.[13,14] Density reconstructions were later explored using diffraction tomography methods,[15] with some researchers developing similar approaches with both algebraic[16] and Fourier-based[17] algorithms. However, the fact that these works are based on linearized scattering theory limits their applicability.

Some inverse scattering methods designed to recover density information have also been developed. Two classes of algorithms have been identified: (1) the separation of sound speed and density contributions from reconstructions

[a]Electronic mail: lavarell@illinois.edu

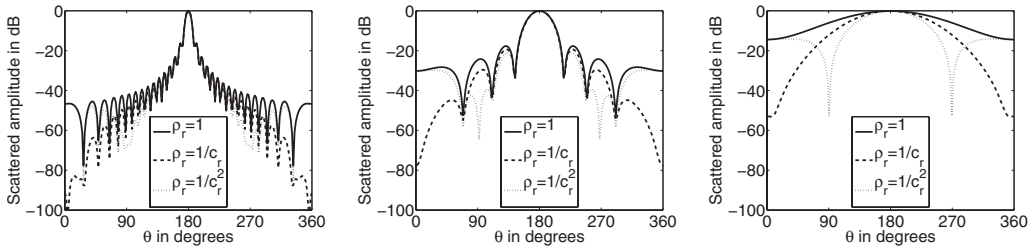

FIG. 1. Effect of ρ_r on the scattered pressure patterns of circular cylinders with $\Delta c=2\%$. All plots show the normalized amplitude of the scattered pressure in decibels. The radii of the cylinders are 4λ (left), λ (center), and λ/4 (right), respectively.

using constant density inverse scattering algorithms at multiple frequencies[18,19] and (2) the inversion of the full wave equation including density changes.[20–22] All of these works claim that UCT can also be used to obtain quantitative images of density distributions.

The goal of the present work is to analyze through simulations the performance of the two classes of variable density inverse scattering algorithms when reconstructing circular cylinders. The effects of scatterer size, density and speed of sound contrast values, and noise are considered. The root mean square error (RMSE) of the reconstructed profiles is used as a quality metric when assessing the accuracy of both approaches. As a result of this work, the fundamental limitations of variable density inverse scattering methods will be better understood and presented in a more comprehensive manner.

The remainder of this paper is organized as follows. Section II reviews the effects of changes in density in the pressure field scattered by a circular cylinder. The performances of the first and the second class of algorithms are analyzed in Sec. III [dual frequency DBIM (DF-DBIM) approach] and Sec. IV (*T*-matrix approach), respectively. Finally, Sec. V discusses the results obtained in this work.

II. EFFECTS OF DENSITY IN THE PRESSURE FIELD SCATTERED BY A CIRCULAR CYLINDER

The analytic solution for the scattering of a cylindrical wave by a circular cylinder is well documented in literature,[23] which allows the generation of exact data for all methods tested in the present work. Consider the case of a cylinder of radius a, density ρ, compressibility κ, speed of sound c, wave number k, and acoustic impedance Z embedded in a homogeneous background. Throughout the present work, for a given acoustical property X, the relative X_r and contrast ΔX values are defined as $X_r=X/X_0$ and $\Delta X=X_r-1$, respectively, where X_0 is the value of the property in the background. The pressure scattered by the cylinder when a line source is located at $x=R$ can be written as

$$p^{sc}(\boldsymbol{r}) = \sum_{m=0}^{\infty} A_m R_m(\kappa,\rho) H_m^{(1)}(k_0 R) H_m^{(1)}(k_0 r) \cos m\theta, \qquad (1)$$

where r and θ are the cylindrical coordinates of the observation point, $A_0=1$ and $A_m=2$, $m>0$, and $H_m^{(1)}(\cdot)$ is the mth order Hankel function of the first kind. The scattering coefficient $R_m(\cdot)$ can be calculated as

$$R_m(\kappa,\rho) = \frac{\frac{1}{Z_r} J_m(k_0 a) J_m'(ka) - J_m(ka) J_m'(k_0 a)}{J_m(ka) H_m'^{(1)}(k_0 a) - \frac{1}{Z_r} J_m'(ka) H_m^{(1)}(k_0 a)}, \qquad (2)$$

where $J_m(\cdot)$ is the mth order Bessel function and the $'$ symbol represents derivative with respect to the total argument. In the Rayleigh limit ($\lambda \gg a$) the scattered pressure in the far field can be approximated as

$$p^{sc}(\boldsymbol{r}) \xrightarrow[\lambda \gg a]{} \frac{k_0 a^2}{2} \frac{e^{ik_0(R+r)}}{\sqrt{Rr}} \left\{ [\kappa_r - 1] - 2 \left[\frac{\rho_r - 1}{\rho_r + 1} \right] \cos\theta \right\}. \qquad (3)$$

The first term in the brackets in Eq. (3) represents monopole scattering with dependence on κ and the second term represents dipole scattering with dependence on ρ.

The effects of density variations on the scattering patterns of circular cylinders with three different radii are shown in Fig. 1. The cylinders had radii λ/4, λ, and 4λ with a fixed speed of sound contrast $\Delta c=2\%$. Three cases were evaluated per cylinder size: $\rho_r=1$ (no changes in density), $\rho_r=1/c_r$ (equal changes in compressibility and density), and $\rho_r=1/c_r^2$ (no changes in compressibility). The pressure fields for each case are shown in Fig. 1. The RMSEs between the $\rho_r=1$ and $\rho_r=1/c_r$ cases were 1.86%, 7.77%, and 31.46% for $a=4\lambda$, λ, and λ/4, respectively. Similarly, the RMSEs between the $\rho_r=1$ and $\rho_r=1/c_r^2$ cases were 3.72%, 15.58%, and 62.93%, respectively. These results illustrate the fact that unless $a \ll \lambda$, the scattered field will be fairly insensitive in the mean square sense to changes in density for low contrast scatterers when $\Delta\rho$ is not much larger than Δc.

III. VARIABLE DENSITY AND THE DBIM

The first class of algorithms for density reconstruction is based on the separation of c and ρ contributions from reconstructed profiles obtained using constant density inversion algorithms at two frequencies. This approach is analogous to the one presented in Refs. 15 and 16 for the diffraction tomography case and was proposed in Ref. 18 using the alternating variable algorithm.[24] Preliminary but limited results using Newton-type methods can be found in Ref. 19. The DBIM,[4] one of the most well-studied constant density inverse scattering methods, will be used for the remainder of this section.

A. The distorted Born iterative method

The details of DBIM are presented here for completeness. The wave propagation in an inhomogeneous medium is described by[25]

$$\rho(\boldsymbol{r})\,\nabla\cdot[\rho^{-1}(\boldsymbol{r})\,\nabla p(\boldsymbol{r})]+k^2(\boldsymbol{r})p(\boldsymbol{r})=-\phi^{\mathrm{inc}}(\boldsymbol{r}), \tag{4}$$

where $p(\boldsymbol{r})$ is the acoustical pressure and $\phi^{\mathrm{inc}}(\boldsymbol{r})$ is the acoustic source. By applying the change of variables $p(\boldsymbol{r})=f(\boldsymbol{r})\rho^{1/2}(\boldsymbol{r})$,[26,27] Eq. (4) can be rewritten as

$$\nabla^2 f(\boldsymbol{r})+(k^2(\boldsymbol{r})-\rho^{1/2}(\boldsymbol{r})\nabla^2\rho^{-1/2}(\boldsymbol{r}))f(\boldsymbol{r})=-\Phi^{\mathrm{inc}}(\boldsymbol{r}). \tag{5}$$

Equation (5) can be expressed in the integral form

$$p(\boldsymbol{r})=e_s(\boldsymbol{r})+\int_{\Omega} d\boldsymbol{r}'\,\mathcal{O}(\boldsymbol{r}')p(\boldsymbol{r}')G_0(\boldsymbol{r},\boldsymbol{r}'), \tag{6}$$

where $e_s(\boldsymbol{r})$ is the incident field caused by a source located at $\boldsymbol{r}_s$, $s=0,1,\ldots,N_s$, and $G_0(\boldsymbol{r},\boldsymbol{r}')=(i/4)H_0^{(1)}(k_0|\boldsymbol{r}-\boldsymbol{r}'|)$ is the Green's function in cylindrical coordinates. The object function $\mathcal{O}$ is given by

$$\mathcal{O}(\boldsymbol{r})=(k^2(\boldsymbol{r})-k_0^2)-\rho^{1/2}(\boldsymbol{r})\nabla^2\rho^{-1/2}(\boldsymbol{r}). \tag{7}$$

Equation (6) can be discretized using the method of moments (MoMs) and written in matrix form, both for the pressure field inside the computational domain $\bar{p}$ and the scattered field outside the computational domain $\bar{p}^{\mathrm{sc}}$, as

$$\bar{p}=(\bar{I}-\bar{C}\cdot\mathcal{D}(\bar{\mathcal{O}}))^{-1}\cdot\bar{p}^{\mathrm{inc}}, \tag{8}$$

$$\bar{p}^{\mathrm{sc}}=\bar{D}\cdot\mathcal{D}(\bar{\mathcal{O}})\cdot\bar{p}, \tag{9}$$

where $\bar{D}$ is a matrix with the Green's coefficients from each pixel to the receivers, $\bar{C}$ is a matrix with the Green's coefficients among all the pixels, and $\mathcal{D}$ is an operator that transforms a vector into a diagonal matrix.

In order to reconstruct the object function from the scattered field data, an iterative algorithm is used. A trial $\bar{\mathcal{O}}_{(0)}$ is chosen for which the corresponding scattered field is calculated. Next, the object function is updated as $\bar{\mathcal{O}}_{(n+1)}=\bar{\mathcal{O}}_{(n)}+\Delta\bar{\mathcal{O}}_{(n)}$, where $\Delta\bar{\mathcal{O}}_{(n)}$ is given by the regularized optimization problem

$$\Delta\mathcal{O}_{(n)}=\arg\min_{\Delta\mathcal{O}}\|\Delta\bar{p}^{\mathrm{sc}}-\bar{F}_{(n)}\cdot\Delta\mathcal{O}\|_2^2+\gamma\|\Delta\mathcal{O}\|_2^2, \tag{10}$$

where $\Delta\bar{p}^{\mathrm{sc}}$ contains the difference between the predicted and measured scattered fields and γ is the regularization parameter. The Frechet derivative matrix $\bar{F}_{(n)}$ is composed of N_s stacked matrices $\bar{F}_s$ of the form[5]

$$\bar{F}_s=\bar{D}\cdot\{\bar{I}-\mathcal{D}(\bar{\mathcal{O}})\cdot\bar{C}\}^{-1}\cdot\mathcal{D}(\bar{p}_s). \tag{11}$$

The iterative process is repeated until the residual error (RRE), given by $\mathrm{RRE}=\|\Delta\bar{p}^{\mathrm{sc}}\|_2/\|\bar{p}^{\mathrm{sc}}\|_2$, falls within a desired termination tolerance. The regularization parameter was chosen using an extension of the approach presented in Ref. 9,

$$\gamma=0.5\sigma_0^2\max\{10^{\log_2\mathrm{RRE}},10^{-4}\}, \tag{12}$$

where σ_0^2 is the square of the dominant singular value of $\bar{F}_{(n)}$ calculated using the Rayleigh quotient iteration.

The DBIM diverges when the magnitude of the excess phase $\Delta\phi$ accumulated by the acoustic wave when traveling through the scatterer approaches π.[24] For a homogeneous circular cylinder, $\Delta\phi$ can be estimated as

$$\Delta\phi=2k_0a(c_r^{-1}-1). \tag{13}$$

This adimensional quantity will be used for the remainder of this work to report the c_r values for different cylinders.

B. The DF-DBIM approach

From Eq. (5), a linear combination of the reconstructions $\mathcal{O}_i$ at frequencies ω_i, $i=1,2,\ldots,N_f$, allows the separation of c and ρ contributions. Specifically,

$$\mathcal{F}_\rho(\boldsymbol{r})=\frac{(\Sigma_{i=1}^{N_f}\omega_i^2)(\Sigma_{i=1}^{N_f}\omega_i^2\mathcal{O}_i(\boldsymbol{r}))-(\Sigma_{i=1}^{N_f}\omega_i^4)(\Sigma_{i=1}^{N_f}\mathcal{O}_i(\boldsymbol{r}))}{N_f\Sigma_{i=1}^{N_f}\omega_i^4-(\Sigma_{i=1}^{N_f}\omega_i^2)^2}, \tag{14}$$

where $\mathcal{F}_\rho=\rho^{1/2}(\boldsymbol{r})\nabla^2\rho^{-1/2}(\boldsymbol{r})$. The simplest approach, the DF-DBIM, is to use $N_f=2$ because for a fixed spatial resolution (dictated by the maximum frequency f_0 used) only one parameter (the lowest frequency $f_{\min}$ used) has to be chosen. To obtain ρ profiles using DF-DBIM, the differential equation

$$\nabla^2 u(\boldsymbol{r})-\mathcal{F}_\rho(\boldsymbol{r})u(\boldsymbol{r})=\mathcal{F}_\rho(\boldsymbol{r}),\quad \boldsymbol{r}\in\Omega,$$

$$u(\boldsymbol{r})=0,\quad \boldsymbol{r}\notin\Omega \tag{15}$$

has to be solved, where $u(\boldsymbol{r})=(\rho_r^{-1/2}(\boldsymbol{r})-1)$. Equation (15) was solved by converting it to a matrix equation, with ∇^2 implemented using a finite difference template.

The effect of some parameters in the quality of ρ reconstructions is shown in Fig. 2. The minimum frequency $f_{\min}$ was varied between $0.9f_0$ and $0.1f_0$, the DBIM termination tolerance was set to 0.1%, and cylinders with radii of λ_0, $2\lambda_0$, and $4\lambda_0$ were reconstructed, where $\lambda_0=c_0/f_0$. Both the dependence on the value of ρ_r compared to c_r (fixed $\Delta\phi=0.9\pi$ and ρ_r values of $1/c_r$, $1/c_r^2$, and $1/c_r^4$) and $\Delta\phi$ (fixed $\rho_r=1/c_r$ and $\Delta\phi$ values of -0.9π, 0.45π, and -0.45π) were studied. For illustration, ρ profiles corresponding to $\Delta\phi=0.9\pi$ and $\rho_r=1/c_r$ are shown in Fig. 3. Larger density changes required the use of lower $f_{\min}$ values for optimum accuracy at the cost of reduced spatial resolution. In general, larger cylinder radii resulted in more unstable reconstructions when f_0 and $f_{\min}$ were relatively close. Therefore, the optimum $f_{\min}$ value depends on the actual imaging target, but results suggest that reliable results can only be obtained when $f_{\min}$ is small compared to f_0.

The effect of the DBIM termination tolerance was also studied. Figure 4 shows the RMSE curves when reconstructing an $a=2\lambda_0$, $\rho_r=1/c_r$, and $\Delta\phi=0.9\pi$ cylinder using tolerances of 0.1%, 1%, and 2%. The RMSE curves behave smoothly when the DBIM tolerance is low (0.1%) but degrade significantly as the tolerance increases unless $f_{\min}\ll f_0$. This behavior has a direct impact in practical imaging

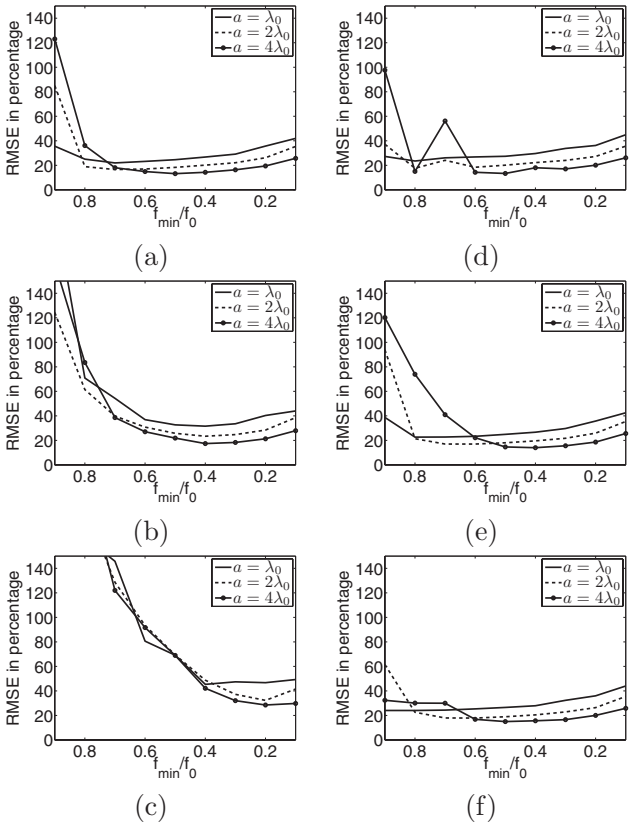

FIG. 2. RMSEs in density reconstructions using the DF-DBIM approach. The corresponding properties of the cylinders are (a) $\rho_r=1/c_r$, $\Delta\phi=0.9\pi$, (b) $\rho_r=1/c_r^2$, $\Delta\phi=0.9\pi$, (c) $\rho_r=1/c_r^4$, $\Delta\phi=0.9\pi$, (d) $\rho_r=1/c_r$, $\Delta\phi=-0.9\pi$, (e) $\rho_r=1/c_r$, $\Delta\phi=0.45\pi$, and (f) $\rho_r=1/c_r$, $\Delta\phi=-0.45\pi$. The DBIM termination tolerance was set to 0.1%.

scenarios because DBIM has to be truncated when the RRE falls below the noise floor to avoid divergence.[4]

It should be emphasized that the RMSE curves are not shown with the intention of identifying an optimum $f_{\min}$ value. In fact, the results from Fig. 2 suggest that several choices of $f_{\min}$ provide solutions with very similar RMSE values. All cases explored, including imaging target and termination tolerance variations, point to using low auxiliary frequencies (less than $0.5f_0$) which limits the spatial resolution of the algorithm. Regardless, the large sensitivity to termination tolerance makes the results provided by DF-DBIM unreliable and therefore alternatives to stabilizing this algorithm need to be studied.

C. DF-DBIM and total variation regularization

Regularization can be used to stabilize the separation of speed of sound and density profiles. One common approach is the generalized Tikhonov regularization, which consists of solving the optimization problem[28]

$$\hat{u} = \arg\min_{\bar{u}} \|\bar{F}_\rho - \bar{G}\cdot\bar{u}\|_2^2 + \gamma\sum_{i=1}^{N}(|(\bar{L}\cdot\bar{u})_i|^2+\beta)^{k/2}, \quad (16)$$

where $\bar{u}$ is a vector representation of $u(\boldsymbol{r})$, $\bar{F}_\rho$ is a vector with the values of $\mathcal{F}_\rho(\boldsymbol{r})$, $\bar{G}=(\mathcal{L}-\mathcal{D}(\bar{F}_\rho))$, $\mathcal{L}$ is the Laplacian matrix, and β is a small positive constant ($\beta=10^{-10}$) introduced to avoid gradient singularities. The solution $\hat{u}$ of Eq. (16) is given by

$$\hat{u} = [(\bar{G}^H\cdot\bar{G} + \gamma\bar{L}^H\cdot\mathcal{D}(\bar{W}_\beta(\hat{u}))\cdot\bar{L})^{-1}\bar{G}^H]\bar{F}_\rho, \quad (17)$$

where $\bar{W}_\beta(\hat{u})_i=(k/2)((|(\bar{L}\cdot\hat{u})_i|^2+\beta)^{1-k/2})$. In particular, total variation (TV) regularization ($k=1$ and L equal to the gradient operator)[29] was explored. For each value of $f_{\min}$ several γ values were used and the optimum reconstruction was selected based on RMSE minimization. It should be emphasized that in real applications the selection of γ becomes an important issue because the ideal object function is not available.

It was found through simulations that even though TV was able to improve on the reconstructions of single cylinders with termination tolerances below 2%, either slightly larger tolerances or more complicated scatterer geometries resulted in eventual divergence due to the inherent sensitivity of DF-DBIM to the termination tolerance. This is illustrated in Fig. 5 for the reconstruction of a concentric cylinder phantom, for which the analytic scattering solution is available.[9] The radii and Δc of the inner and outer cylinders were λ_0 and -10% and $2\lambda_0$ and -5%, respectively. In both cylinders, $\rho_r=1/c_r$. The termination tolerance was set to 5%, higher than in previous examples.

Even though TV regularization improved upon the nonregularized inversion as reported in Fig. 5, the performance was still unsatisfactory as evidenced by the large RMSEs (larger than 40% for all cases). A sample reconstruction using DF-DBIM is shown in Fig. 5(b) using $f_{\min}=0.4f_0$. When regularization is not used, spurious slopes appeared in ideally homogeneous regions, which is the cause of the large RMSE. TV regularization helps in reducing these artifacts and improving the RMSE, but the reconstruction error is still fairly large. When using very low frequencies ($f_{\min}=0.2f_0$), the effect of TV regularization was negligible and the optimum reconstruction was similar to the one obtained with no regularization. Therefore, TV is an aid but not a complete solution to the DF-DBIM robustness problem, and further algorithmic developments are required to reduce the sensitivity of DF-DBIM prior to applying TV regularization.

IV. *T*-MATRIX APPROACH FOR DENSITY IMAGING

The second class of algorithms consists of directly inverting the full wave equation including changes in ρ. Implementations include the use of MoM formulations,[20] *T*-matrix approaches,[21] and contrast source inversion methods.[22,30] The work in Ref. 30 only deals with the case of constant κ. Of the other approaches, the *T*-matrix method in Ref. 21 was chosen as representative for this class of algorithms because it is the only work, to the authors' knowledge, that went as far as providing experimental reconstructions.

A. Theoretical background

The details of the *T*-matrix algorithm are presented in Ref. 21. The computational domain is divided in N homoge-

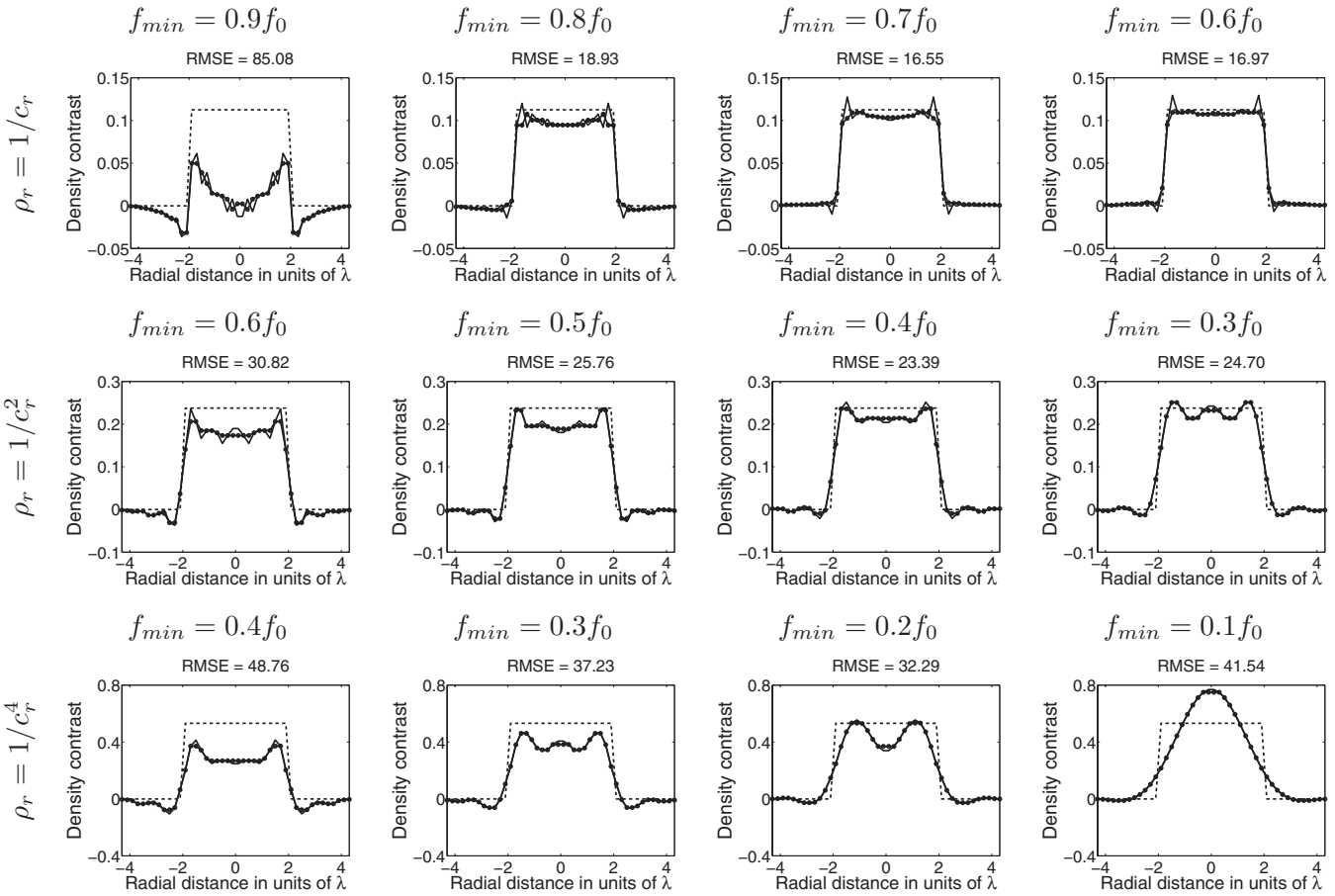

FIG. 3. Reconstruction of ρ profiles of cylinders with $\Delta\phi=0.9\pi$ and radius $2\lambda_0$ using DF-DBIM. The reconstructed (solid), ideal (dashed), and median filtered (dotted) profiles are shown. The DBIM termination tolerance was set to 0.1%.

neous subscatterers distributed on a rectangular grid of pixel size h. The total acoustic field produced at some point $\boldsymbol{r}_p$ in space is given by

$$p(\boldsymbol{r}_p) = \psi(\boldsymbol{r}_p - \boldsymbol{r}_s) \cdot \bar{f}_s + \sum_{m=1}^{N} \psi(\boldsymbol{r}_p - \boldsymbol{r}_m) \cdot \bar{a}_m, \tag{18}$$

where $\boldsymbol{r}_s$ is the location of the source, $\boldsymbol{r}_m$ is the location of the mth subscatterer, $\psi(\boldsymbol{r})$ is a vector of cylindrical harmonics, and $\bar{f}_s$ and $\bar{a}_m$ are vectors containing the amplitudes of the cylindrical harmonic fields generated by the source and the mth subscatterer, respectively.

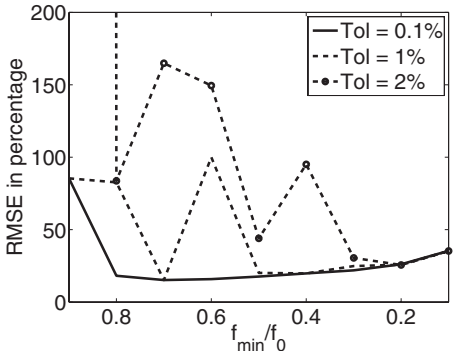

FIG. 4. Effect of the DBIM termination tolerance by reconstructing a cylinder with radius $2\lambda_0$. $\rho_r=1/c_r$, and $\Delta\phi=0.9\pi$ using termination tolerances of 0.1%, 1%, and 2%.

The equation above can be rewritten using the jth subscatterer as the origin for all the cylindrical harmonics using the addition theorem of Bessel functions[31] as

$$p(\boldsymbol{r}_p) = \psi(\boldsymbol{r}_{pj}) \cdot \bar{a}_j + \hat{\psi}(\boldsymbol{r}_{pj}) \cdot \left(\sum_{m \neq j} \bar{\alpha}_{jm} \cdot \bar{a}_m + \bar{e}_{js} \right),$$

$$[\alpha_{jm}]_{kl} = H_{k-l}^{(1)}(k_0|\boldsymbol{r}_{mj}|) e^{-i(k-l)\theta_{mj}}, \tag{19}$$

where $[\hat{\psi}(\boldsymbol{r})]_k = J_k(k_0 r)e^{il\theta}$ and, for line sources, $[\bar{e}_{js}]_k = H_k^{(1)} \times (k_0|\boldsymbol{r}_{sj}|)e^{-ik\theta_{sj}}$. If $h \ll \lambda$, the harmonics $l=0,1,-1$ are sufficient to characterize the scattering process. The vector of equivalent induced sources $\bar{a}_s$ when the transmitter is at the position $\boldsymbol{r}_s$ is approximated as

$$\{\bar{I} - \mathcal{D}(\bar{R}) \cdot \bar{A}\} \cdot \bar{a}_s = \mathcal{D}(\bar{R}) \cdot \bar{e}_s, \tag{20}$$

where $\bar{A}$ is a matrix containing the $[\alpha_{jm}]_{kl}$ coefficients, $\mathcal{D}(\bar{R})$ is a diagonal matrix with the reflection coefficients given by Eq. (2) using a pixel radius $a=h/\sqrt{\pi}$ for the harmonics $k=0,1,-1$, and $\bar{e}_s$ is a vector whose elements are given $\bar{e}_{js}$. If the total pressure $\bar{e}_{ts}$ at the scatterer is defined such that $\bar{a}_s = \mathcal{D}(\bar{R}) \cdot \bar{e}_{ts}$, then from Eq. (20),

$$\bar{e}_{ts} = [\bar{I} - \bar{A} \cdot \mathcal{D}(\bar{R})]^{-1} \cdot \bar{e}_s. \tag{21}$$

The T-matrix formulation can be inverted using the same iterative process used in the DBIM. The object function

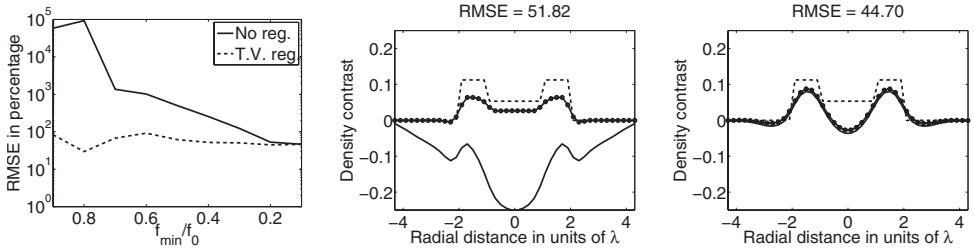

FIG. 5. Reconstructions of $\Delta\rho$ profiles of a concentric cylinder phantom using DF-DBIM and TV. The DBIM termination tolerance was set to 5%. The RMSE curves both without (solid) and with (dashed) TVs are shown in (a). Reconstructions using $f_{\min}=0.4f_0$ (b) and $f_{\min}=0.2f_0$ (c) are also shown. In (b) and (c), the ideal (dashed) and reconstructed profiles both with (dotted) and without (solid) TV regularizations are shown.

vector is here defined as $\mathcal{O}=[\{\bar{R}\}_{k=0};\{\bar{R}\}_{k=1}]$ because $R_1(\kappa,\rho)=R_{-1}(\kappa,\rho)$. By analogy with Eq. (11), the Frechet derivative matrix blocks $\bar{F}_s$ are given by

$$\bar{F}_s = \bar{\psi}\cdot\{\bar{I}-\mathcal{D}(\bar{R})\cdot\bar{A}\}^{-1}\cdot\mathcal{M}(\bar{e}_{ts}), \tag{22}$$

$$\mathcal{M}(\bar{e}_{ts}) = \begin{bmatrix} \mathcal{D}(\{\bar{e}_{ts}\}_{k=0}) & 0 \\ 0 & \mathcal{D}(\{\bar{e}_{ts}\}_{k=1}) \\ 0 & \mathcal{D}(\{\bar{e}_{ts}\}_{k=-1}) \end{bmatrix}. \tag{23}$$

B. Convergence of the *T*-matrix algorithm using single frequency data

The T-matrix approach was used to reconstruct ρ and κ profiles of homogeneous circular cylinders with radius 2λ and $\Delta\phi=0.9\pi$. Four cases were considered: $\rho_r=1$, $\rho_r=1/c_r$, $\rho_r=1/c_r^2$, and $\rho_r=1/c_r^4$. The results are shown in Fig. 6. It can be observed that the mean reconstructed density value ρ_m did not significantly change among all cases despite the fact that the true values changed over a large range. This is due to the fact that the scatterer was not small compared to the wavelength and therefore the scattered field was mainly dominated by the changes in c, which was held constant for all simulations. For all simulations c was the only parameter reconstructed with good numerical accuracy.

Given that the mean reconstructed compressibility κ_m and density ρ_m converge in the mean to the same values, it is of interest to analyze the characteristics of the expected reconstructed profiles for κ and ρ. If the c contrast dominates the scattering, c_r will be properly reconstructed and all candidate solutions should satisfy $\kappa_r\rho_r=1/c_r^2$. For homogeneous objects, the candidate object function can be represented by the 2×1 vector $\hat{\mathcal{Q}}(\kappa_r,\rho_r)=[R_0(\kappa_r,\rho_r),R_1(\kappa_r,\rho_r)]$. Given that the algorithm solves for the object function in the least squares sense, the quantities $\hat{\kappa}$ and $\hat{\rho}$ defined as

$$\hat{\kappa},\hat{\rho} = \arg\min_{\kappa_r,\rho_r}\{\|\hat{\mathcal{O}}\|^2\} \quad \text{subject to } \kappa_r\rho_r=\frac{1}{c_r^2} \tag{24}$$

are an approximation of the minimum norm solution of the inversion problem, and therefore it is expected that κ_m and ρ_m should correlate with these quantities when using an all-zero initial guess.

Several simulations were performed in order to study the behavior of the pairs (κ_m,ρ_m) and $(\hat{\kappa},\hat{\rho})$ using cylinders of radii $2\lambda_0$ and $4\lambda_0$ as imaging targets. The speed of sound

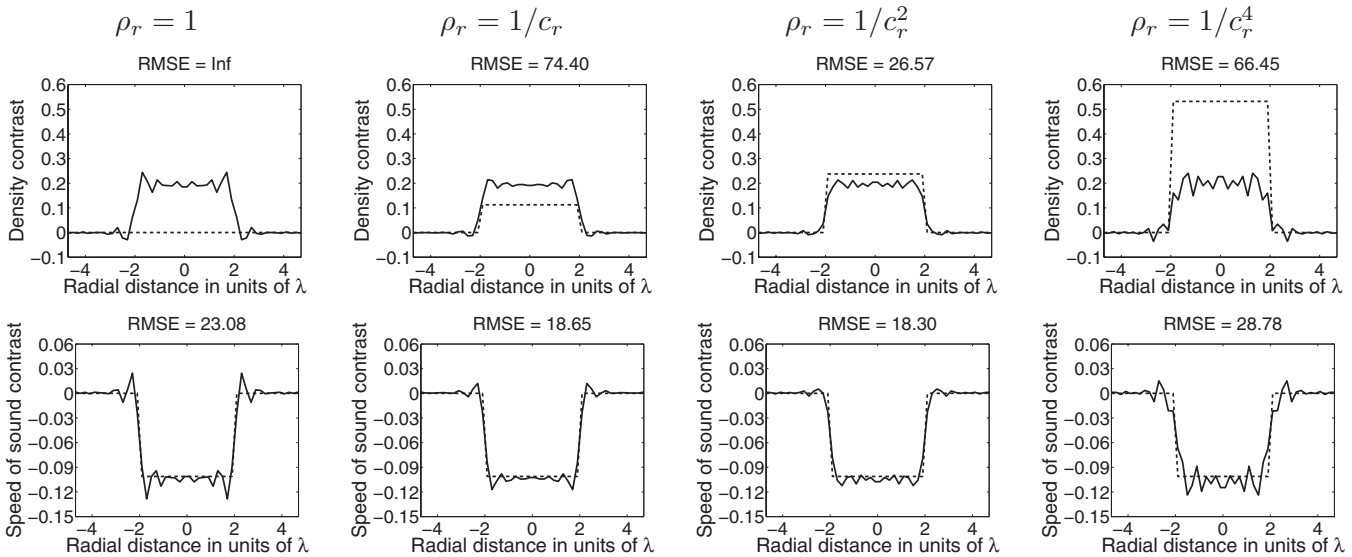

FIG. 6. Reconstructions of 2λ radius cylinders with $\Delta\phi=0.9$ using the single frequency T-matrix approach. First column: $\rho_r=1$. Second column: $\rho_r=1/c_r$. Third column: $\rho_r=1/c_r^2$. Fourth column: $\rho_r=1/c_r^4$. Both the reconstructed (solid) and ideal (dashed) profiles are shown. The T-matrix termination tolerance was set to 2%.

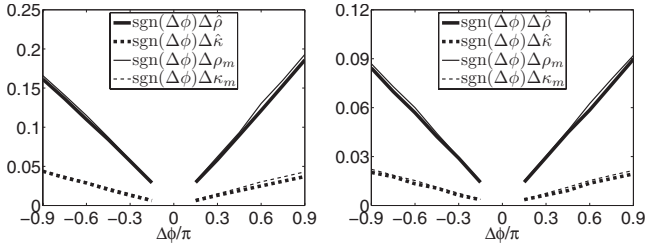

FIG. 7. Mean reconstructed excess density ρ_m and compressibility κ_m values and the corresponding $\hat{\kappa}$ and $\hat{\rho}$ values when reconstructing $2\lambda_0$ (left) and $4\lambda_0$ (right) radii cylinders with different speed of sound values.

contrast for each cylinder size was changed so that the excess phase $\Delta\phi$ ranged between -0.9π and 0.9π. The point $\Delta\phi=0$ was excluded because it would imply $c_r=1$, and therefore density changes only govern the scattering process. The ρ_m and κ_m values were calculated from tomographic reconstructions using scattered data corresponding to $\rho_r=1/c_r$ ($2\lambda_0$ radii cylinders) and $\rho_r=1/c_r^2$ ($4\lambda_0$ radii cylinders). The $\hat{\kappa}$ and $\hat{\rho}$ values for each case were estimated using an exhaustive search in the interval $\kappa_r \in [0.8, 1.2]$. The results are shown in Fig. 7. The mean error between the reconstructed mean density contrast ρ_m and the corresponding minimum norm solution $\hat{\rho}$ was only 4.1% for the $2\lambda_0$ cylinders and 3.9% for the $4\lambda_0$ cylinders, which indicates a high correlation between the two quantities.

C. Convergence of the *T*-matrix algorithm using multiple frequency data

As observed in Sec. II, the dependence of the scattered field on density changes becomes more significant for low frequencies. Therefore, the use of multiple frequencies may improve the convergence of the *T*-matrix approach, which has been briefly explored in Ref. 21. The multiple frequency data were processed using the frequency hopping approach,[6] i.e., the sequential use of progressively larger frequencies to refine the inverse scattering reconstructions. The frequency hopping profiles were obtained using all frequencies $f=2^{-m}f_0$, $m=M-1, M-2, \ldots, 0$, where M and f_0 are the number of frequencies and the maximum frequency used in the reconstructions, respectively.

First, a set of simulations was performed to reconstruct cylinders of radii λ_0, $2\lambda_0$, and $4\lambda_0$. For all simulations, $\Delta\phi=0.9\pi$ and $\kappa_r=\rho_r$. The reconstructions were obtained using minimum frequencies $f_{\min}$ ranging between $f_0/2$ and $f_0/64$. The reconstructed density profiles are shown in Fig. 8. The RMSE in the ρ reconstructions initially decreases with decreasing $f_{\min}$. However, at some point the improvement stops and the RMSE starts to increase slowly. For the analyzed cases, the best ρ reconstructions in terms of the RMSE occurred when $f_{\min}=(\lambda_0/8a)f_0$ was used.

The trend observed in the cases analyzed in Fig. 8 indicates that the ability of the *T*-matrix approach using fre-

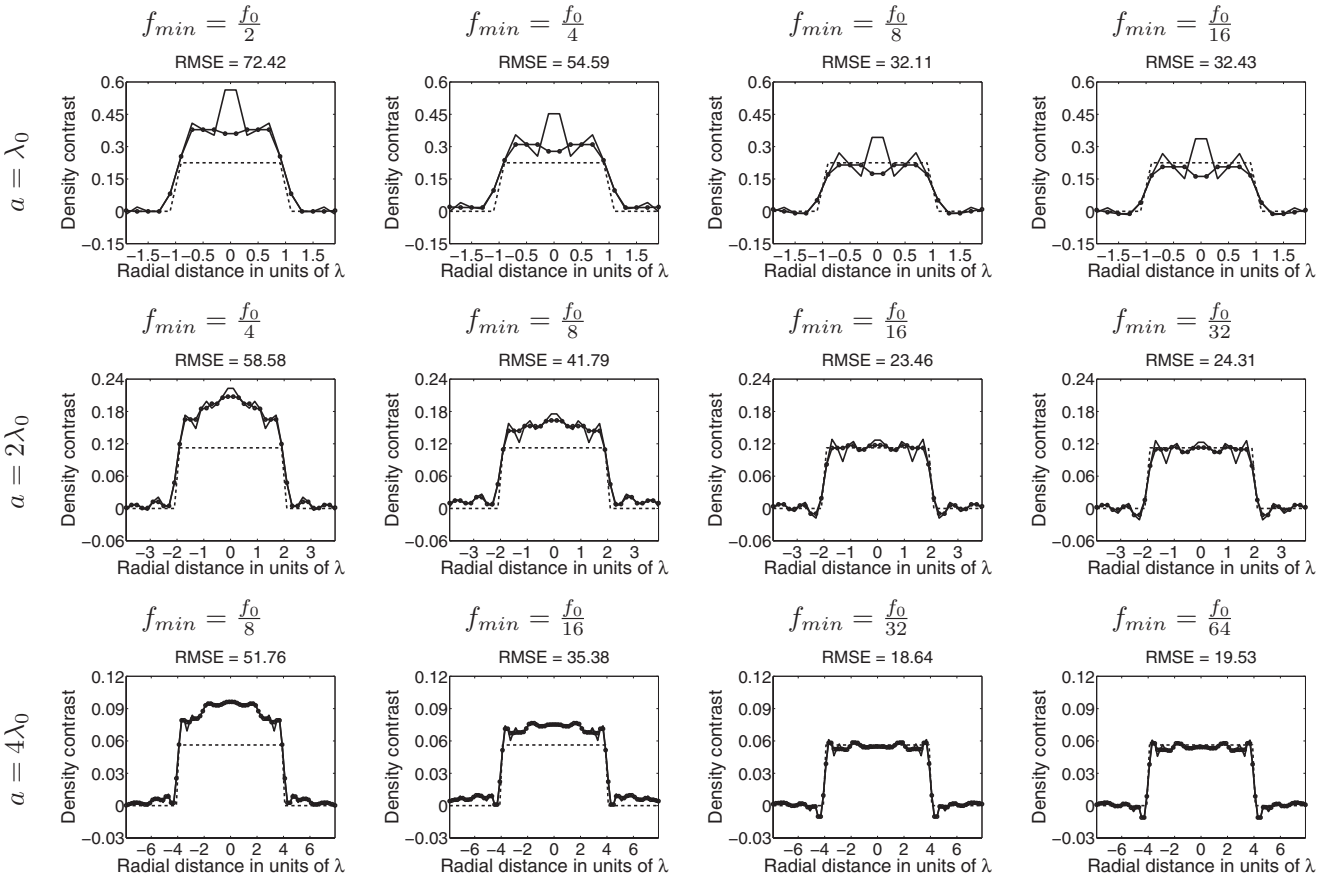

FIG. 8. Frequency hopping reconstructions using the *T*-matrix approach for cylinders with a fixed excess phase $\Delta\phi=0.9\pi$ and $\rho_r=1/c_r$. The reconstructed (solid), ideal (dashed), and median filtered (dotted) density profiles are shown. The reported RMSE values correspond to the nonfiltered reconstructions. The *T*-matrix termination tolerance was set to 2%.

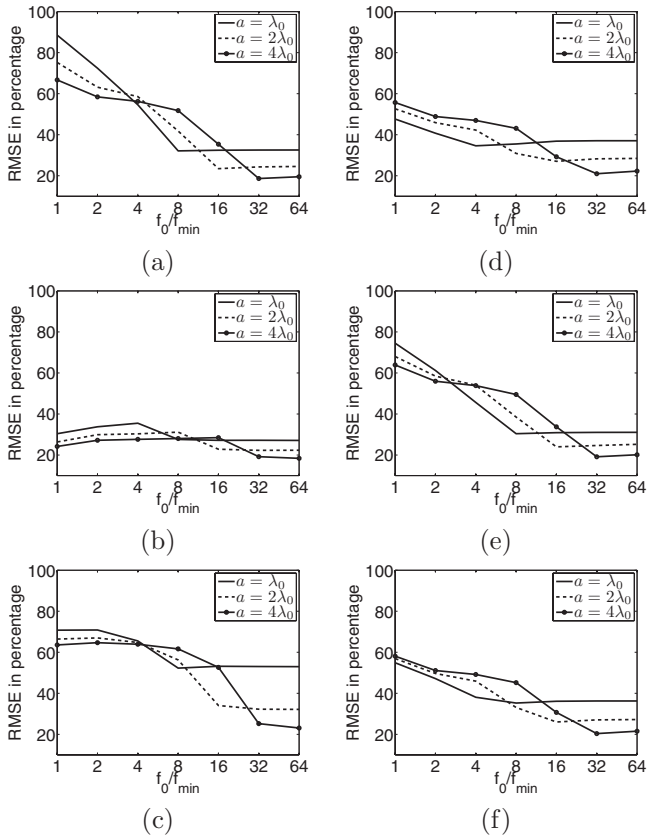

FIG. 9. RMSEs in density reconstructions using frequency hopping and the *T*-matrix approach. The corresponding properties of the cylinders are (a) $\rho_r=1/c_r$, $\Delta\phi=0.9\pi$, (b) $\rho_r=1/c_r^2$, $\Delta\phi=0.9\pi$, (c) $\rho_r=1/c_r^4$, $\Delta\phi=0.9\pi$, (d) $\rho_r=1/c_r$, $\Delta\phi=-0.9\pi$, (e) $\rho_r=1/c_r$, $\Delta\phi=0.45\pi$, and (f) $\rho_r=1/c_r$, $\Delta\phi=-0.45\pi$. The *T*-matrix termination tolerance was set to 2% for all simulations.

quency hopping works only if the cylinder radius is small compared to the maximum λ used. In order to verify that such a trend indeed exists, the behavior of the RMSE in the reconstructed $\Delta\rho$ using the same simulation sets as in Sec. III B was studied. The results are presented in Fig. 9. For all cases, the scatterer size was the main factor that affected the reconstruction quality.

V. DISCUSSION

The results from Secs. III and IV suggest that both the DF-DBIM and *T*-matrix algorithms were able to generate density images with RMSE values lower than 30% when reconstructing cylinders up to eight wavelengths in diameter with moderate density changes, provided that certain requirements related to the imaging apparatus [i.e., signal-to-noise ratio (SNR) and bandwidth] were met. These requirements and their implications for the experimental implementations of these algorithms are discussed below.

A. DF-DBIM approach

The DF-DBIM approach is severely affected by inaccuracies of reconstructions performed at any one frequency. Even in the absence of noise, the denominator of Eq. (14) is very small when f_0 and $f_{\min}$ are too close to each other and therefore numerical errors are amplified. On the other hand, when $f_0 \gg f_{\min}$, density reconstructions will suffer from spatial resolution degradation because of the limited spectral support of the far-field measurements.[32]

Simulation results suggest that the performance of DF-DBIM depends on properties of the imaging target that are not known *a priori*, i.e., ρ_r. However, the main drawback of the technique is its sensitivity to the termination tolerance of the single frequency DBIM reconstructions. Even for low termination tolerances (1%–2%), the RMSE curves become highly irregular, as shown in Fig. 2. This further complicates the selection of an appropriate $f_{\min}$, especially for real applications in which the SNR dictates the minimum tolerance that can be used in the reconstructions. The limited results presented here suggest that reconstructions using very low $f_{\min}$ values are less sensitive to changes in the termination tolerance.

TV regularization was also briefly explored as a means to improve the performance of the DF-DBIM approach. TV may help improve the reconstruction error, but even with the use of TV, DF-DBIM was plagued by its large sensitivity to the DBIM termination tolerance. Further algorithmic developments may be tested to ameliorate the performance of this approach given its potential to obtain density information using relatively small bandwidths (less than an order of magnitude) which may readily be obtainable with current transducer technology.

B. *T*-matrix approach

The *T*-matrix approach fails to converge when the scatterer size a is of moderate size compared to λ because the scattering pattern is dominated in the mean square sense by c variations rather than the actual values of κ and ρ, as illustrated in Fig. 1. As a becomes smaller than λ, scattering theory predicts that the scattered pressure pattern becomes more sensitive to the actual values of κ and ρ. This explains why the use of frequency hopping with minimum frequencies such that $ka \approx 1$ resulted in accurate ρ reconstructions. However, using even lower frequencies did not help improve the accuracy of the inversions. This is expected from the results of Sec. II because when $ka \ll 1$, the scattered pressure pattern reaches the asymptotic Rayleigh regime given by Eq. (3) and no further information is obtained.

For a homogeneous cylinder of radius a, divergence in c can be avoided by the use of frequencies low enough such that[24]

$$k_0 a < \frac{\pi}{2}\frac{c_r}{|c_r - 1|}. \tag{25}$$

Density imaging using the *T*-matrix approach diverges due to a different mechanism, namely, the weak dependence of the scattering pattern on ρ for large ka values. The convergence condition can be approximated as $ka < 1$. Therefore, for all practical biomedical imaging applications the condition for *T*-matrix convergence in κ and ρ is more restrictive than the one for DBIM convergence in c. Convergence in the reconstruction in c_r when using the *T*-matrix approach is obtained regardless of the divergence of κ and ρ, as long as the condition in Eq. (25) is satisfied. These results have a profound

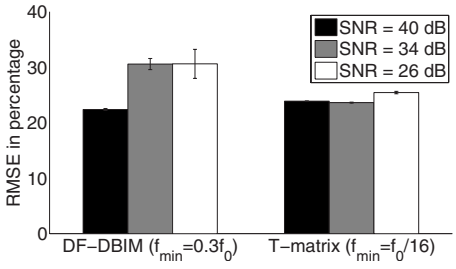

FIG. 10. RMSE in the reconstruction of circular cylinders with $a=2\lambda_0$ and $\rho_r=1/c_r$. The SNRs were set to 40 dB (black bars), 34 dB (gray bars), and 26 dB (white bars), respectively.

impact on the feasibility of the use of the *T*-matrix approach. Even for imaging targets as small as four wavelengths in size ($a=2\lambda_0$) a frequency jump larger than an order of magnitude is needed in order to obtain good numerical accuracy. This requirement becomes more restrictive with increasing target size and severely limits experimental implementations of the algorithm.

Quadratic regularization, which was used in the present work to stabilize the *T*-matrix inversions, is commonly chosen because of simplicity but not because of optimality. Some studies[22,30] suggest that improved results in terms of spatial resolution in variable density inverse scattering can be obtained by using TV regularization. This approach has also been used in constant density inverse scattering problems.[33] However, it remains to be studied if the *T*-matrix bandwidth requirement can be reduced when using this approach.

C. Effects of noise

Additive noise is another practical consideration that has an effect on the quality of the reconstructions. In order to provide a preliminary evaluation of the effects of noise, a cylinder with radius $2\lambda_0$ and $\rho_r=1/c_r$ was reconstructed using both the DF-DBIM and *T*-matrix approaches. The minimum frequencies $f_{\min}$ were chosen using values that provided good reconstructions in Secs. III and IV of the present work: $f_{\min}=0.3f_0$ and $f_{\min}=f_0/16$ for the DF-DBIM and *T*-matrix approaches, respectively. The SNRs were set to 40 dB (1% noise), 34 dB (2% noise), and 26 dB (5% noise). All the reconstructions were stopped when the RRE dropped below the noise level. Twenty-four simulations were conducted for each setting with different zero-mean, Gaussian noise realizations. The mean and standard deviation of the reconstruction RMSEs are shown in Fig. 10.

The small variation in both the mean and variance of the RMSEs as a function of the noise level for the *T*-matrix approach suggests that the technique is reasonably robust to noise. The mean RMSEs for the DF-DBIM case are very close to the ones obtained in Sec. III B, which suggests that the RMSEs are mainly biased by the termination tolerance. The variance induced by the noise itself was not too large compared to the mean RMSE values, although it was larger than the one for the *T*-matrix reconstructions especially for smaller SNR values. Based on diffraction tomography studies[15] it could be expected that DF-DBIM is a noise sensitive technique. However, in the present case f_0 is large compared to $f_{\min}$ which keeps the noise from being significantly amplified. In addition, the DBIM profiles were obtained using a regularized algorithm that efficiently reduces reconstruction fluctuations due to noise in the measurements.

VI. CONCLUSIONS

The present work presents several contributions to the field of inverse scattering. The most important contribution is the joint performance analysis of two inverse scattering algorithms (DF-DBIM and *T*-matrix) designed to reconstruct density profiles. The performances of both approaches were studied under different conditions considering the effects of the cylinder size relative to the acoustic wavelength, density contrast, and speed of sound contrast.

Second, this work suggests that the performance of the DF-DBIM algorithm is severely affected by the termination tolerance of the single frequency DBIM reconstructions. The use of TV regularization improved the performance of DF-DBIM but was not enough to guarantee convergence to a proper solution for moderate termination tolerances. Further improvements may be studied in order to increase the robustness of this algorithm.

Third, this work indicated that the single frequency *T*-matrix algorithm only provides accurate reconstructions of speed of sound, as long as speed of sound dominates scattering over density contributions. This condition is met for targets of moderate to large sizes ($ka>1$) even when density and speed of sound contrasts are comparable. Even further, the profiles to which density and compressibility reconstructions converge in the single frequency case were successfully characterized.

Finally, the convergence criteria for the multiple frequency *T*-matrix algorithm were found through simulations to be mainly affected by the imaging target size. The minimum frequency required to obtain accurate density reconstructions must satisfy $ka<1$. This constraint is more severe than the one for speed of sound reconstructions and was related to the insensitivity of scattering patterns to density variations for large *ka* values. This algorithm may require an excessively large bandwidth to reconstruct the density profile of large targets. Further studies are required to investigate if variations in the algorithm allow a reduction in the bandwidth required for convergence.

In summary, neither algorithm appears amenable for direct experimental implementation. Their fundamental limitations, presented here in a cohesive manner, will serve as reference points for further algorithmic improvements required for practical experimental implementation of density imaging on ultrasound tomographic systems.

ACKNOWLEDGMENTS

The authors would like to thank Dr. S. Bond for discussions on the DF-DBIM algorithm. This work was supported in part by a grant from the 3M Corporation.

[1]J. Greenleaf, S. Johnson, S. Lee, G. Herman, and E. Wood, "Algebraic reconstruction of spatial distributions of acoustic absorption within tissue from their two-dimensional acoustic projections," Acoust. Hologr. **5**, 591–603 (1974).

[2]J. Greenleaf, S. Johnson, W. Samayoa, and F. Duck, "Algebraic reconstruction of spatial distributions of acoustic velocities in tissue from their time-of-flight profiles," Acoust. Hologr. **6**, 71–90 (1975).
[3]B. Robinson and J. Greenleaf, "The scattering of ultrasound by cylinders: Implications for diffraction tomography," J. Acoust. Soc. Am. **80**, 40–49 (1986).
[4]W. C. Chew and Y. M. Wang, "Reconstruction of two-dimensional permittivity distribution using the distorted Born iterative method," IEEE Trans. Med. Imaging **9**, 218–225 (1990).
[5]D. Borup, S. Johnson, W. Kim, and M. Berggren, "Nonperturbative diffraction tomography via Gauss-Newton iteration applied to the scattering integral equation," Ultrason. Imaging **14**, 69–85 (1992).
[6]W. C. Chew and J. H. Lin, "A frequency-hopping approach for microwave imaging of large inhomogeneous bodies," IEEE Microw. Guid. Wave Lett. **5**, 440–441 (1995).
[7]S. A. Goss, R. L. Johnston, and F. Dunn, "Comprehensive compilation of empirical ultrasonic properties of mammalian tissues," J. Acoust. Soc. Am. **64**, 423–457 (1978).
[8]S. A. Goss, R. L. Johnston, and F. Dunn, "Compilation of empirical ultrasonic properties of mammalian tissues II," J. Acoust. Soc. Am. **68**, 93–108 (1980).
[9]R. J. Lavarello and M. L. Oelze, "A study on the reconstruction of moderate contrast targets using the distorted Born iterative method," IEEE Trans. Ultrason. Ferroelectr. Freq. Control **55**, 112–124 (2008).
[10]S. A. Johnson, T. Abbott, R. Bell, M. Berggren, D. Borup, D. Robinson, J. Wiskin, S. Olsen, and B. Hanover, "Noninvasive breast tissue characterization using ultrasound speed and attenuation," Acoust. Imaging **28**, 147–154 (2007).
[11]M. L. Oelze, W. D. O'Brien, Jr., J. P. Blue, and J. F. Zachary, "Differentiation and characterization of rat mammary fibroadenomas and 4T1 mouse carcinomas using quantitative ultrasound imaging," IEEE Trans. Med. Imaging **23**, 764–771 (2004).
[12]J. Mamou, M. L. Oelze, W. D. O'Brien, Jr., and J. F. Zachary, "Identifying ultrasonic scattering sites from three-dimensional impedance maps," J. Acoust. Soc. Am. **117**, 413–423 (2005).
[13]S. J. Norton, "Generation of separate density and compressibility images in tissue," Ultrason. Imaging **5**, 240–252 (1983).
[14]S. Mensah and J. P. Lefebvre, "Enhanced compressibility tomography," IEEE Trans. Ultrason. Ferroelectr. Freq. Control **44**, 1245–1252 (1997).
[15]A. J. Devaney, "Variable density acoustic tomography," J. Acoust. Soc. Am. **78**, 120–130 (1985).
[16]M. Moghaddam and W. Chew, "Variable density linear acoustic inverse problem," Ultrason. Imaging **15**, 255–266 (1993).
[17]M. A. Anastasio, D. Shi, and T. Deffieux, "Image reconstruction in variable density acoustic tomography," Proc. SPIE **5750**, 326–331 (2005).
[18]M. J. Berggren, S. A. Johnson, B. L. Carruth, W. W. Kim, F. Stenger, and P. K. Kuhn, "Ultrasound inverse scattering solutions from transmission and/or reflection data," Proc. SPIE **671**, 114–121 (1986).
[19]S. Kwon and M. Jeong, "Ultrasound inverse scattering determination of speed of sound, density and absorption," Proc.-IEEE Ultrason. Symp. **2**, 1631–1634 (1998).
[20]S. A. Johnson and F. Stenger, "Ultrasound tomography by Galerkin or moment methods," in *Lecture Notes in Medical Informatics*, edited by O. Nalcioglu and Z. Cho (Springer-Verlag, New York, NY, 1984), Vol. 23, pp. 254–275.
[21]J. Lin and W. Chew, "Ultrasonic imaging by local shape function method with CGFFT," IEEE Trans. Ultrason. Ferroelectr. Freq. Control **43**, 956–969 (1996).
[22]K. W. A. van Dongen and W. M. D. Wright, "A full vectorial contrast source inversion scheme for three-dimensional acoustic imaging of both compressibility and density profiles," J. Acoust. Soc. Am. **121**, 1538–1549 (2007).
[23]T. Cavicchi and W. D. O'Brien, Jr., "Acoustic scattering of an incident cylindrical wave by an infinite circular cylinder," IEEE Trans. Ultrason. Ferroelectr. Freq. Control **35**, 78–80 (1988).
[24]T. Cavicchi, S. Johnson, and W. D. O'Brien, Jr., "Application of the sinc basis moment method to the reconstruction of infinite circular cylinders," IEEE Trans. Ultrason. Ferroelectr. Freq. Control **35**, 22–33 (1988).
[25]P. M. Morse and K. U. Ingard, *Theoretical Acoustics* (McGraw-Hill, Princeton, NJ, 1968).
[26]S. A. Johnson, F. Stenger, C. Wilcox, J. Ball, and M. J. Berggren, "Wave equations and inverse solutions for soft tissue," Acoust. Imaging **11**, 409–424 (1982).
[27]S. Pourjavid and O. J. Tretiak, "Numerical solution of the direct scattering problem through the transformed acoustical wave equation," J. Acoust. Soc. Am. **91**, 639–645 (1992).
[28]W. C. Karl and M. Cetin, "Feature-enhanced synthetic aperture radar image formation based on nonquadratic regularization," IEEE Trans. Image Process. **10**, 623–631 (2001).
[29]R. Akar and C. R. Vogel, "Analysis of bounded variation penalty methods for ill-posed problems," Inverse Probl. **10**, 1217–1229 (1994).
[30]G. Pelekanos, A. Abubakar, and P. M. van den Berg, "Contrast source inversion methods in elastodynamics," J. Acoust. Soc. Am. **114**, 2825–2834 (2003).
[31]W. C. Chew, *Waves and Fields in Inhomogeneous Media* (IEEE, Piscataway, NJ, 1995).
[32]T. J. Cui, W. C. Chew, X. X. Yin, and W. Hong, "Study of resolution and super resolution in electromagnetic imaging for half-space problems," IEEE Trans. Antennas Propag. **52**, 1398–1411 (2004).
[33]X. Zhang, S. Broschat, and P. Flynn, "A comparison of material classification techniques for ultrasound inverse imaging," J. Acoust. Soc. Am. **111**, 457–467 (2002).